Journal of Fluids and Structures 18 (2003) 63–77

JOURNAL OF
FLUIDS AND
STRUCTURES

www.elsevier.nl/locate/jnlabr/yjfls

Dynamic aero-structural response of an elastic wing model

M. Kämpchen[a,]*, A. Dafnis[a], H.-G. Reimerdes[a], G. Britten[b], J. Ballmann[b]

[a] *Department of Aerospace and Lightweight Structures, Aachen University (RWTH), Wüllnerstr. 7, D-52062 Aachen, Germany*
[b] *Department of Mechanics, Aachen University (RWTH), Templergraben 64, D-52062 Aachen, Germany*

Received 26 March 2003; accepted 16 July 2003

Abstract

A highly elastic rectangular wing model with a supercritical airfoil was designed and manufactured to study aero-structural equilibrium configurations and aerodynamic damping at various speeds in a subsonic wind tunnel. The supporting structure is a cross-shaped spar. A foam with negligible stiffness is used to provide the aerodynamic surface of the wing. Experimental data are used to examine a coupled algorithm for simulating fluid–structure interaction which simultaneously solves the Euler or Navier–Stokes equations and the structural dynamics equations in the time domain. The elastic wing is modelled by a generalized Timoshenko-type beam with six degrees of freedom for a material cross-section. Correct reproduction of the aero-structural equilibrium shape of the wing model and the deflection under zero lift and nonzero lift conditions, time consistency of unsteady deformations and pressure fluctuations are examined by comparing numerical and experimental results.

1. Introduction

The paper describes work performed in the collaborative research center SFB 401 "*Flow Modulation and Fluid–Structure Interaction at Airplane Wings*" of the Aachen University (RWTH), Aachen, Germany. The aerodynamic loads acting on the wings of a high capacity aircraft—e.g., with a wing span of up to 80 m—may cause large displacements of the wing sections. Therefore, the static and dynamic interaction between structural loads and air loads become more important than in the case of aircraft currently in use. New computational aeroelasticity (CA) design tools which take into account the full nonlinear fluid–structure interaction may help to avoid unnecessary loops in the design process since even the first drafts with reduced structural models can already lead to desirable results. This would help to meet economic demands for faster and cheaper design and construction.

These new CA codes which are currently being developed call for a set of elastic 3D wing models suitable for conducting wind tunnel experiments (subsonic, transonic) to provide data for validating aerodynamic codes. Due to the limited number of elastic wing models for public aero-structural research (at least in Europe), one objective of the collaborative research center SFB 401 is to create a Benchmark Models Program (BMP) of highly elastic wings suitable for aero-structural and aeroelastic wind tunnel investigation. The main aim here is to produce a set of models including both simple wing shapes (3D straight wing, 3D back-swept constant chord wing) and more complex wing configurations typical for modern transport aircraft. At NASA Langley Research Center, a comparable BMP was founded during the 1990s for evaluating of new codes for computational aeroelasticity (Bennett et al., 1991; Bennett and Edwards, 1998). Wing model research derived from this BMP also focuses on enhancing the understanding of the physics of unsteady flow and providing data for empirically based designs.

---

*Corresponding author. Tel.: +49-241-8096840; fax: +49-241-80-92230.
E-mail address: kaempchen@ifl.rwth-aachen.de (M. Kämpchen).

0889-9746/$ - see front matter © 2003 Elsevier Ltd. All rights reserved.
doi:10.1016/S0889-9746(03)00090-2

The method of choice in this paper is direct aeroelastic simulation, i.e., calculation of the flow field and structural deformation is done fully coupled and time consistently. The aerodynamic part of the numerical method for solid fluid interaction (SOFIA) presented in this paper consists of either an implicit Euler or Navier–Stokes code. A finite-element-based solver for a multi-axial Timoshenko beam model is used to discretize the elastic wing structure. SOFIA is being developed, validated and employed at the Collaborative Research Center SFB 401 (RWTH, Aachen, Germany) in a mutual exchange with experimental aeroelasticity projects. This paper focuses on the comparison of numerical and experimental results for aero-structural equilibrium configurations and aero-structural dynamics of a rectangular elastic wing at low flow speeds.

2. Wing models under wind tunnel conditions

2.1. Numerical simulations

2.1.1. Nonstationary flow in a moving grid

The flow field is calculated by integrating the Navier–Stokes equations for unsteady compressible fluid flow. The governing equations are solved by finite volume techniques with time-dependent control volumes in order to consistently describe the fluid flow about the wing being deformed and the corresponding movement of the wing surface. Thus, the flow mesh nodes on the wing surface are taken as material points of the wing throughout the motion of the structure, whereas the nodes at the outer flow field boundary, which is the far field boundary of the computational domain, remain fixed in a rigid-body fixed coordinate system. Thus, the grid is deformed over time and the nodes of the finite volumes within the flow field are moved such as to ensure that the grid fits the surface. For a nonrotating reference frame and in finite volume form, the three-dimensional Reynolds-averaged Navier–Stokes equations used in the FLOWer code read

$$\frac{\partial}{\partial t}\int_{V(t)} \boldsymbol{U}\,\mathrm{dV} + \int_{\partial V(t)} (\boldsymbol{F}^c + \boldsymbol{F}^d)\boldsymbol{n}\,\mathrm{dS} = 0, \tag{1}$$

where $\boldsymbol{U} = (\rho, \rho u, \rho v, \rho w, \rho e)^{\mathrm{T}}$ is the algebraic vector of the conserved mass density, Cartesian components of momentum density and total specific energy density. The flux function $\boldsymbol{F}^c$ contains the convective terms including pressure in a time-dependent reference frame, with coordinate lines being deformed (velocity $\boldsymbol{v}_B$) according to the wing deformation. $\boldsymbol{F}^d$ denotes the dissipative flux,

$$\boldsymbol{F}^c = \begin{bmatrix} \rho(\boldsymbol{v}-\boldsymbol{v}_B) \\ \rho u(\boldsymbol{v}-\boldsymbol{v}_B) + p\boldsymbol{e}_x \\ \rho v(\boldsymbol{v}-\boldsymbol{v}_B) + p\boldsymbol{e}_y \\ \rho w(\boldsymbol{v}-\boldsymbol{v}_B) + p\boldsymbol{e}_z \\ \rho e(\boldsymbol{v}-\boldsymbol{v}_B) + p\boldsymbol{v} \end{bmatrix}, \qquad \boldsymbol{F}^d = \begin{bmatrix} 0 \\ \tau_{xx}\boldsymbol{e}_x + \tau_{xy}\boldsymbol{e}_y + \tau_{xz}\boldsymbol{e}_z \\ \tau_{yx}\boldsymbol{e}_x + \tau_{yy}\boldsymbol{e}_y + \tau_{yz}\boldsymbol{e}_z \\ \tau_{zx}\boldsymbol{e}_x + \tau_{zy}\boldsymbol{e}_y + \tau_{zz}\boldsymbol{e}_z \\ \psi_x\boldsymbol{e}_x + \psi_y\boldsymbol{e}_y + \psi_z\boldsymbol{e}_z \end{bmatrix}. \tag{2}$$

It is assumed that air behaves as a perfect gas. The pressure can then be calculated using the ideal gas equation of state in terms of pressure, density and internal energy

$$p = (\kappa - 1)\rho(e - \tfrac{1}{2}\boldsymbol{v}^2) \tag{3}$$

with κ denoting the constant ratio of specific heats.

Kroll et al. (2000) give a detailed description of the dissipative part, including the formulation of the symmetrical stress tensor components, with Stokes' hypothesis of vanishing pressure viscosity ($\mu_v = \frac{2}{3}\mu$). In the case of laminar flow, viscosity is approximated as a function of static temperature only by Sutherland's formula:

$$\mu(T) = \frac{\sqrt{\kappa}M_\infty}{\mathrm{Re}_\infty}\left(\frac{T}{T_\infty}\right)^{3/2}\frac{T_\infty + 110\ \mathrm{K}}{T + 110\ \mathrm{K}}. \tag{4}$$

The heat conduction vector is modelled according to Fourier's law ($\boldsymbol{q} = -k$ grad T), with the heat conductivity k calculated with a constant Prandtl number Pr

$$k = \frac{\kappa}{\kappa - 1}\frac{\mu}{Pr}, \quad \mathrm{Pr} = 0.72. \tag{5}$$

For turbulent flow, viscosity μ is replaced by $\mu + \mu_t$, with the turbulent portion provided by a turbulence model.

2.1.2. Beam theory

The elastic wing is currently modelled in SOFIA using a Timoshenko beam structure with six degrees of freedom for a material cross-section represented by the three translational degrees of freedom of its mass center and the three rotational degrees of freedom of the cross-section. The aerodynamic profile of the cross-section is assumed to remain constant. The center-lines of mass, bending and torsion are generally noncoincident. Taking this for granted, and assuming aerodynamic coupling, all degrees of freedom may also be coupled mechanically with each other. Unlike the commonly used Euler–Bernoulli beam theory, which couples bending with translation by kinematic constraint and thus involves anomalous dispersion of deformation energy propagation, the Timoshenko approximation, with two additional degrees of freedom for shear deformation, shows no anomalous dispersion effect and so gives a physically sound description for unsteady deformation.

Adding to Hamilton's principle for the wing the virtual work of air loads δW^{aero}, the terms for the initial conditions δZ_{IC} and the boundary conditions δZ_{BC} as well as a Lagrangian term δZ_C for additional masses like winglets and engines, yields the variational equation

$$\delta I^e(\boldsymbol{u}_S, \boldsymbol{\varphi}) = \int_{t_0}^{t_e} \left(\delta \int_0^l l_B \, \mathrm{d}\xi + \delta W^{\text{aero}} \right) Dt + \delta Z_C + \delta(Z_{IC} + Z_{BC}), \tag{6}$$

from which, using the secondary conditions $\delta \boldsymbol{u}_S(\xi, t_e) = \boldsymbol{0}$ and $\delta \boldsymbol{\varphi}(\xi, t_e) = \boldsymbol{0}$, the entire initial boundary value problem of the structural portion can be derived. $\boldsymbol{u}_S$ and $\boldsymbol{\varphi}$ denote the displacement vector of the cross-sectional mass center and the rotation vector of the material cross-section, with the coordinate ξ at time t. This yields the Lagrangian density

$$l_B = \tfrac{1}{2}(\rho_L \dot{\boldsymbol{u}}_S \dot{\boldsymbol{u}}_S + \dot{\varphi} \boldsymbol{\Theta}_S \dot{\boldsymbol{\varphi}} - GA\boldsymbol{\gamma}\boldsymbol{K}\boldsymbol{\gamma} - EAu^2_{B1|1} - \boldsymbol{\varphi}_{|1} \boldsymbol{C}_{BTW} \boldsymbol{\varphi}_{|1} + \rho_L \boldsymbol{u}_S \boldsymbol{g}), \tag{7}$$

the dots denoting time derivatives, ρ_L the mass per unit length, $\boldsymbol{\Theta}_S$ the mass inertia tensor, $GA\boldsymbol{K}$ the shear stiffness tensor, $\boldsymbol{\gamma}$ the shear angle, EA the tension stiffness, u_{B1} the axial displacement of the bending center $\boldsymbol{B}$, $\boldsymbol{C}_{BTW}$ the bending torsion stiffness tensor, and $\boldsymbol{g}$ the gravity. Index 1 stands for the ξ direction, and index |1 for the differentiation with respect to ξ. Applying Timoshenko's theory, the shear angles are represented as

$$\gamma_2 = u_{S2|1} - \varphi_3 - (\zeta_{SD}\varphi_1)_{|1}, \quad \gamma_3 = u_{S3|1} + \varphi_2 + (\eta_{SD}\varphi_1)_{|1}, \tag{8}$$

where ζ_{SD} and η_{SD} are the Cartesian coordinate differences between the center of gravity and the shear center of the cross-section. Indices 2 and 3 correspond to the directions η and ζ. A detailed description of the model is given by Nellessen (1995).

2.2. Solution strategy

Within SOFIA, independently developed solvers implicit both in time for the flow field and the structure deformation are strongly coupled through an iterative process such as to simultaneously integrate the differential equations for both factors. Due to the deformation, the flow domain is dependent on time, and so flow discretization uses a flexible grid. The central time loop works as follows: One-dimensional structural analysis (ODISA) calculates the velocities and structural displacements under the actual aerodynamic loads. The flow grid points on the wing surface (inner boundary of the aerodynamic grid) are surface-fixed, and therefore move according to the structural change in shape. In contrast to the points at the inner boundary of the flow field, the grid points at its outer boundary are fixed in a rigid-body fixed coordinate system. Grid generator (GRIDGEN) computes the point distribution such as to preserve the topology of the structured grid. Finally, the flow field and the new air loads are computed for the current time on the deformed grid, which is updated concerning position and state of velocity. This is done by the INFLEX code (Brenneis, 1989) solving the Euler equations, or in the new version of SOFIA by the FLOWer code, optionally integrating the Navier–Stokes or the Euler equations on a moving grid (Heinrich et al., 1996).

In a weakly coupled version, the new air-load distribution can be used to proceed in time with the structural deformation in the next physical time step. For strong coupling similar to the staggered algorithms discussed by Farhat and Lesoinne (2000), an iteration technique was used which repeatedly runs through the weak coupling cycle during the same physical time step, thus applying the instantaneous average values of the aerodynamic forces of the current and preceding iteration step (Fig. 1, bottom). The iteration is stopped when a certain error bound is reached. To be sure, the computer time increases linearly with the number of iteration levels. Numerical experiments have shown that in case of carefully chosen time steps—i.e., all time scales resolved correctly—one iteration cycle is sufficient. The numerical methods used in SOFIA are described here only very briefly (for further details, see Britten and Ballmann, 2000, 2001; Heinrich et al., 1996; Nellessen, 1995).

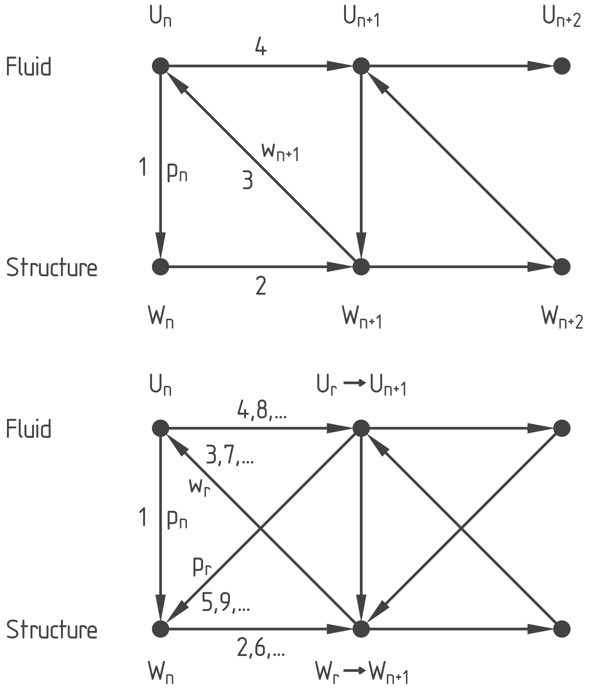

Fig. 1. Scheme for weak (top) and strong (bottom) coupling.

2.2.1. Flow solver FLOWer

As part of the project MEGAFLOW, the FLOWer code is being developed by various German research organizations led by the DLR/Braunschweig (Kroll et al., 2000). The numerical discretization of the FLOWer code is based on structured grids. Central differences are used for spatial discretization. Time integration is performed by dual-time stepping. Within each pseudo-time step, an explicit multi-stage Runge–Kutta algorithm is used which is accelerated by techniques of local pseudo-time stepping, enthalpy damping and implicit residual smoothing. The solution procedure is embedded into a sophisticated multi-grid algorithm. This flow solver is written in a flexible block-structured form, thus allowing complex aerodynamic configurations to be treated with any kind of mesh topology. By coupling a structural solver and an algebraic grid generator (Britten and Ballmann, 1999; Werle, 1997), the code could be applied to aeroelastic analysis.

2.2.2. Structural solver

Inserting a discretization by isoparametric, two-noded elements for the displacement and rotation vectors into Eq. (6), a second-order-in-time system of ordinary differential equations (ODEs) for the six sets of node values for displacements and rotations is derived from Hamilton's principle according to Ritz/Kantorowitsch (Nellessen, 1995). Linear damping is optionally included (Rayleigh damping). A reduced integration scheme is used to prevent shear locking. The set of ODEs is integrated using Newmark's method, where the resulting linear system of equations is solved directly using LU decomposition. The external forces are assumed to vary linearly during a time step. Alternatively, the system of ODEs is diagonalized by solving the generalized eigenvalue problem (EVP), and time integration is done by evaluating Duhamel's integral.

2.3. Elastic wing model for wind tunnel testing

A wealth of data from aero-structural analysis comparing CFD calculations with wind tunnel experiments has been reported over the past few years. Most of the wind tunnel wing models manufactured during the last 15 years were developed in the USA. The widely known wing models used for validation and understanding of physics as well as for evaluating new measurement techniques are the AGARD 445.6 wing (Yates, 1988), the Aeroelastic Research Wing (ARW-2) (Eckstrom et al., 1994) and several wings developed as part of the Benchmark Aeroelastic Models Program (BMP) (Bennett et al., 1991). The structure of most of these bears no resemblance to any original wing configuration (nonscaled models). Another wing model suitable for aero-structural and aeroelastic research for modern transport aircraft is the elastic wing model developed within the frame of the Aeroelastic Model Program (AMP) by Deutsche Airbus (Zingel, 1991). This is an Airbus A340 scaled wing model (1:25). Unfortunately, neither structural properties nor any test results are available for public research. It was therefore necessary to build a set of new elastic 3D wing models suitable for aero-structural and aeroelastic research. These wing models may also help to increase understanding of the effects of unsteady flow interacting with the elastic structure and provide data for empirical design, especially regarding the potential of structural/aeroelastic tailoring.

The first elastic wing models developed at the Department of Aerospace and Lightweight Structures differ in various aspects from the rigid wing models normally used for wind tunnel tests. Due to the significant deformations—especially the twist—under wind-on conditions, the assumption of a rigid wing was not yet valid even during the design process. This is particularly relevant for the angle of attack to be adjusted with reference to the root chord line (root angle of attack) for a wing's total lift of zero. The elastic wing models were designed for both static and dynamic aero-structural behavior. Hence, a wind tunnel must have a low turbulence level to avoid that the turbulence-induced structural response of the elastic wing model will interfere with the measuring signals.

The results reported in this paper were obtained using a rectangular wing model with a half span of 1 m and a chord length of 222 mm. It has the same aspect ratio ($\Lambda = 9$) and the same supercritical airfoil (BAC3-11/RES/30/21) (Moir, 1994) as the reference configuration defined by the Collaborative Research Center (SFB 401) (Özger et al., 2001) (Fig. 2). Unlike scaled wing models, which will be investigated in the future, this model was not required to meet any other similarity criteria.

The following requirements had to be met:

(i) highly deflecting elastic structure (within the limits of the available wind tunnel);
(ii) predefined bending and torsion stiffness, as well as arbitrary stiffness coupling;
(iii) relatively low eigenfrequencies;
(iv) very low structural damping;
(v) free of flutter instabilities;
(vi) possibility to install sensors (strain gauges, pressure transducers, accelerometers).

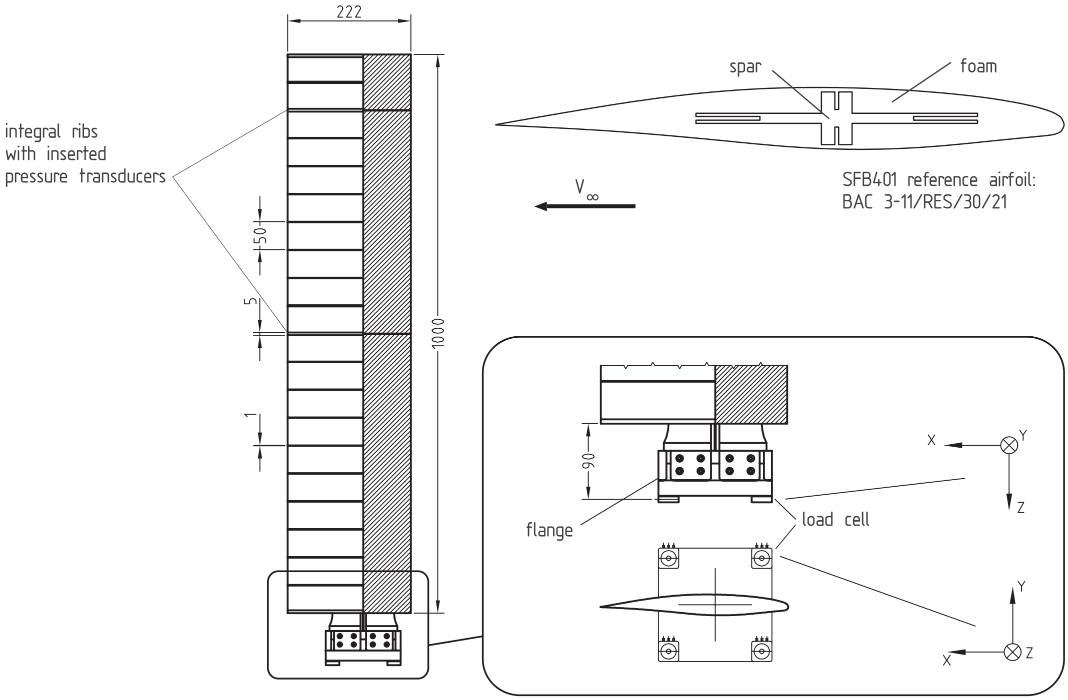

Fig. 2. Plan form of the wing model.

2.3.1. Design, sizing and construction

In view of these requirements, a hybrid structure was preferred unlike the compact design by Lee-Rausch and Batina (1995) and the shaped plate by Bendiksen and Hwang (1997). A model like the MPMM (multi-purpose modular model) by Amiryants and Ishmuratov (2001) did not appear suitable due to the risk of undefined friction between the modules, causing unpredictable damping behavior. Furthermore, a modular model requires a difficult iterative theoretical–experimental procedure in order to predict the stiffness parameters. The rectangular wing model is assembled using the following structural components: (i) load-carrying structure (wing spar); (ii) ribs; (iii) aerodynamic encasement.

The measurement instrumentation was integrated into this assembly. The specific static and dynamic requirements were met via iterative strength/stiffness/mass analysis.

In order to predict the structural behavior of straight and swept wing models in the design phase, a linearized, fast analysis tool was used to provide an iterative approximation for determining the static equilibrium state of the elastic wing under the given flow conditions. Starting with a calculated wing deformation (previous iteration step), the new aerodynamic load distribution can be estimated using the wing shape calculated earlier. At this stage of the structural design of the wing model a vortex lattice method was used to calculate the aerodynamic load distribution. This method yields the air-load distribution values at discrete points which is interpolated to the nodes of the FE model for calculating the new deformation state. This procedure is continued until convergence is reached. For a structural description of the wing, arbitrary finite elements can be applied, such as beam, shell and/or volume elements (Kämpchen et al., 2000, 2001). A cross-shaped wing spar (Fig. 2) was selected, being appropriate to perform the requirements. To initiate both high static elastic deformations and closely coupled eigenmodes regarding response problems due to unsteady aerodynamics, a low torsion stiffness was needed. It was assessed by optimizing the cross-shaped spar varying the dimensions globally and locally (see vertical and horizontal notches). The exact geometry is given in Table 1.

The influence of different materials (steel, titanium, aluminum) on the static and dynamic deformation was assessed during the design process (Dafnis et al., 1998). For the spar of the straight, rectangular wing model treated in this paper, only metallic materials were considered because they show lower structural damping (hysteresis) than do (fiber-reinforced) plastics. Thus the aerodynamic damping became evident. The aluminum alloy FORTAL 7075-T6 was chosen for the wing spar because it shows large deflections without occurrence of plasticity and low structural damping. This elastic wing model was designed for investigating static and dynamic aero-structural response problems in a low-speed wind tunnel at the Aachen University (1.5 m diameter, max. 70 m/s). There should be no aeroelastic phenomena (e.g., divergence, flutter) during the initial stages of research. The wing condition "free of unstable aeroelastic phenomena" was approved by a flutter analysis code using the v-g method developed at the Department of Aerospace and Lightweight Structures (Butt and Dafnis, 1989). Hence, the center-lines of mass, bending and torsion approximately coincide at 40% chord length. The main static and dynamic properties of the wing model (stiffness/mass distribution, eigenmodes) are specified in Section 2.3.2.

The aerodynamic loads were transferred to the wing spar using aluminum ribs and polyurethane integral-foam segments which filled the space between the ribs. A total of 21 ribs was used to ensure cross-section rigidity on the full wing span (inflexible airfoil camber). Nine miniaturized in situ pressure transducers were installed on two of the ribs to directly register transient pressure signals.

The wing spar thickens at the root and is bolted to a rigid flange which is part of a piezoelectric 6-components balance capable of recording the static and dynamic reaction forces/moments at the clamped support. Strain gauges were installed at 16 locations on the wing span to measure bending and torsion strains. The strain gauges were placed on the cross-shaped wing spar such that signal cross-coupling was negligible. The strain gauges allow the material behavior to be monitored during the tests and the wing deflection to be determined under wind-on condition by using load calibration curves obtained during laboratory specification tests (indirect method). Furthermore, 10 very low-mass accelerometers were placed in pairs at 5 locations on the wing span to support the measurement of dynamic response due to transient aerodynamics.

Table 1
Geometry of the wing spar cross-section (mm)

Vertical part			Horizontal part		
Width	Height	Notch	Width	Height	Notch
12	21	1.5×7	110	4	1.5×25

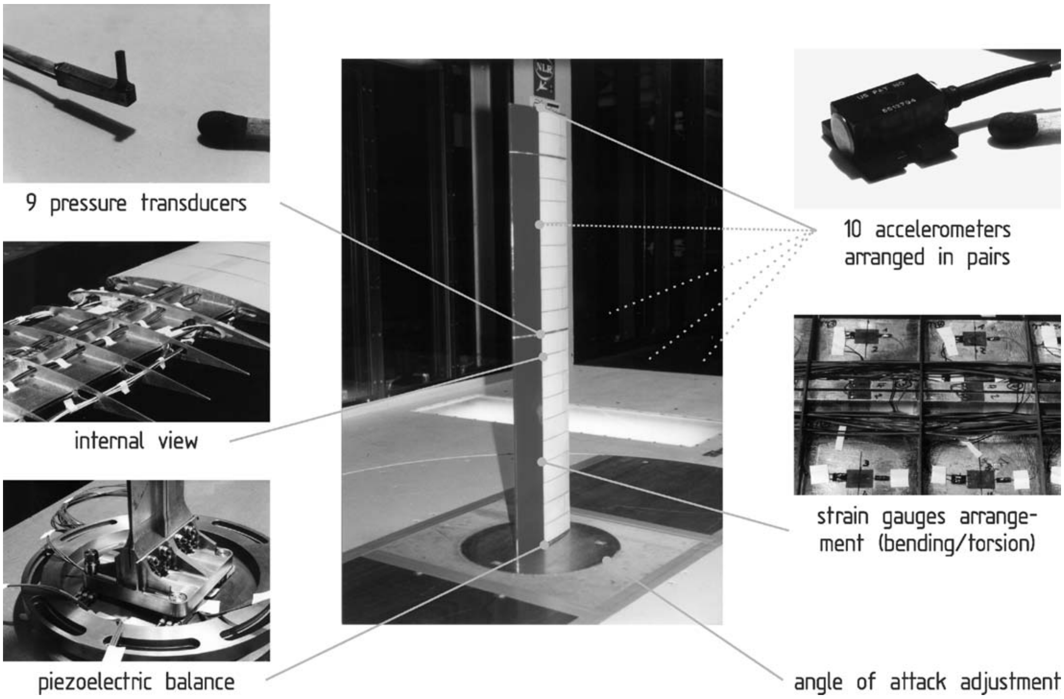

Fig. 3. Measurement equipment.

Fig. 3 shows the measurement equipment used.

2.3.2. *Wind–off structural identification*

A series of laboratory identification tests yielded the following data for the structural properties of the wing model:

(1) bending/torsion stiffness distribution which determines influence-number matrices,
(2) position of the elastic axis,
(3) load calibration curves for reconstructing of the bending/torsion wing deformation under wind-on conditions,
(4) mass distribution including discrete masses (e.g., ribs, foam segments, sensors),
(5) eigenfrequency, eigenform, damping (parametric identification).

Regarding items (1)–(3), a special device was designed for introducing shear forces and pure torsion moments into the wing structure. Displacements were measured in 3D using two draw wire sensors and one laser-optical CCD displacement sensor (triangulation sensor). Table 2 shows the average stiffness.

In this particular wing model, the center lines of bending, torsion and mass approximately coincide at 40% chord length. Experimental modal analysis was carried out by the impact method, yielding modal parameters in a frequency range of up to 300 Hz. Table 3 shows a comparison of the modal parameters measured under wind-off conditions with numerical simulation results for the Timoshenko beam model.

2.3.3. *Wind tunnel testing*

These experiments on highly elastic wing models were carried out to validate the direct aeroelastic simulation method (Section 2.1). Fig. 4 shows the interactive validation process. Items requiring further research are shown in a box drawn with dotted lines. The subject of this paper is "dynamic response problems (unsteady aerodynamics)".

As already mentioned, the elastic wing model was designed for a subsonic wind tunnel at the Aachen University (RWTH). It is a closed-loop atmospheric wind tunnel with an open test section. The initial testing stages were marred by persistent vibration problems, thus making it necessary to average the signals recorded. Due to the disturbed data, particularly for the dynamic response tests, the wind tunnel could not be used for aero-structural validation purposes. Therefore, new tests were conducted at the DNW-LST of the NLR in Emmeloord, a closed-loop atmospheric wind tunnel with a closed-wall test section. Thanks to its low turbulence level ($T_u < 0.03\%$), the problem of the persistent wing vibration was eliminated and the new measurement signals showed a high signal-to-noise ratio.

Table 2
Measured/calculated stiffness (N mm^2)

Flap bending	Lag bending[a]	Torsion
5.864×10^8	2.178×10^{10}	1.4133×10^8

[a] Calculated stiffness.

Table 3
Modal parameters (frequency (Hz), damping (%))

	1st Plunge		2nd Plunge		1st Torsion	
	freq.	damp.	freq.	damp.	freq.	damp.
Experiment	8.88	0.30	54.2	0.11	51.3	0.65
Simulation	8.80	—	53.7	—	51.0	—

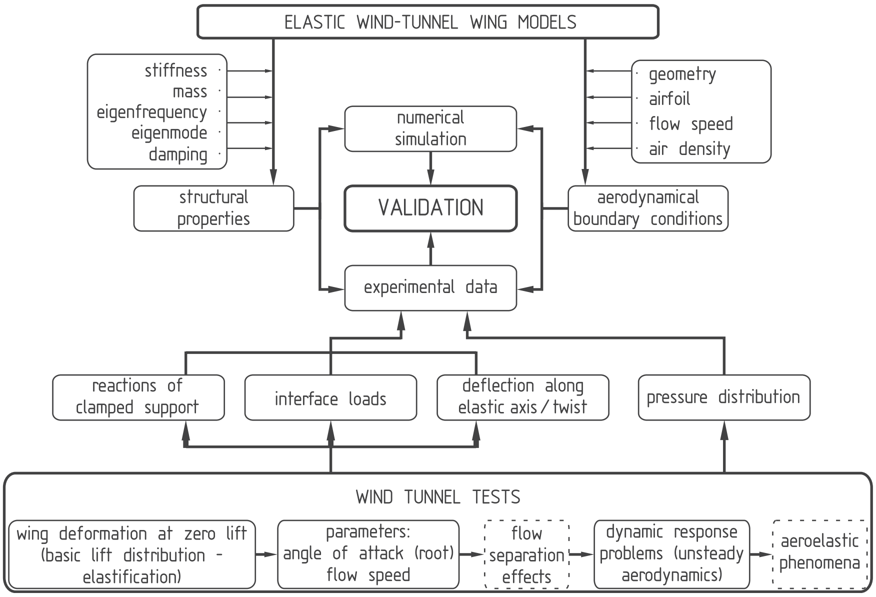

Fig. 4. Outline of the validation process.

When testing highly elastic wing models, the first step is accurate determination of the angle of attack, with reference to the root chord line, at which the total lift equals zero. For a nonsymmetric airfoil like the BAC3-11, the zero lift angle of attack for an elastic wing depends on the flow speed (Fig. 5). It asymptotically approaches the corresponding angle of a rigid wing only if the flow speed tends towards zero. Due to the pitching moment of the nonsymmetric airfoil, the root angle of attack must be raised with increasing flow speed.

Based on the angles of attack determined for zero lift, wind tunnel tests were conducted for additional angles of attack ($\Delta\alpha_r = [-2, 2, 4, 6, 8]^\circ$) at the respective flow speeds ($V_\infty = [25, 35, 45, 55, 65]$ m/s). The angle of attack $\Delta\alpha_r$ represents the difference between the angle adjusted at the wing root and the angle of attack for zero lift measured at the respective flow speed. It was found that there is no flow separation in the investigated field of angles of attack even regarding the elastic twist deformation of the wing model. The signals of the bending and torsion strain gauges, the clamped support reactions, the pressure in one airfoil section and the acceleration at 10 different positions were recorded during all tests with a sample rate of 600 Hz.

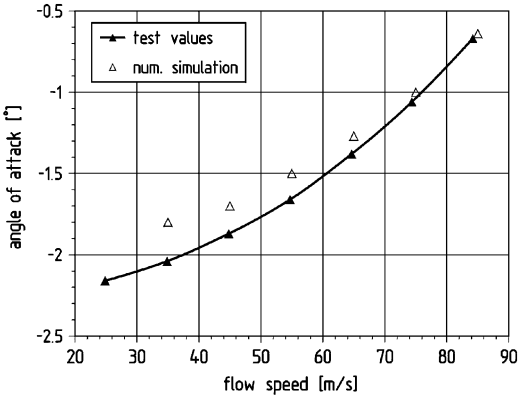

Fig. 5. Root angle of attack of zero lift vs. flow speed.

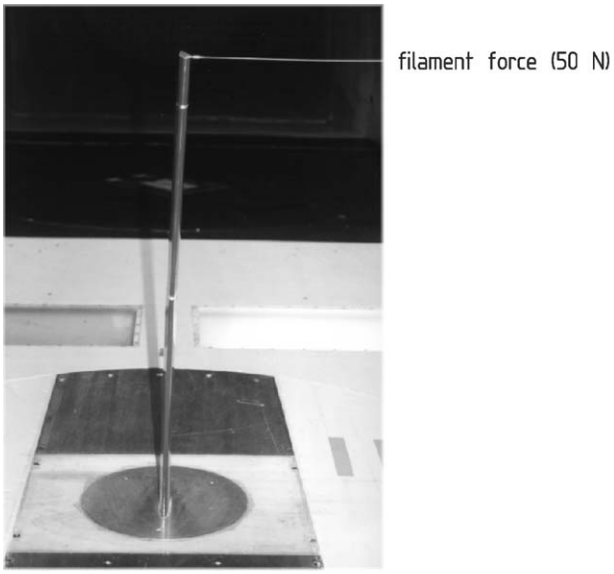

Fig. 6. Test setup for the pluck tests.

Apart from the tests under steady state flow conditions, pluck (removing force) tests were done for most of the aforementioned flow parameters. The experimental setup for all of these tests was the same (Fig. 6):

A thin nylon fiber was attached to the wing tip near the leading edge at 5% chord. Pulling the fiber, the wing model was deflected in bending and torsion. Since the air loads under wind-on conditions further deform the wing model, the fiber force was controlled by a load cell until the desired steady state flow condition was reached. The fiber was then severed by burning, after which the wing model began to vibrate under wind-on conditions with decreasing amplitudes.

The purpose of these tests was to extract the coupling and damping characteristics under wind-on conditions (aerodynamic coupling and damping) for the elastic wind tunnel wing model and to compare the experimental results with the results of the numerical simulation.

3. Results

The standard numerical procedure to determine a wing's steady state aeroelastic equilibrium configuration at a given Mach number and root angle of attack is as follows: First, the fluid flow field about the nondeformed reference configuration is computed. Since for that purpose, the fluid solver can be run uncoupled to the structural part in “steady” mode, the numerical effort for this first step is relatively low. In the second stage, the unsteady flow field about the wing has to be computed running the code in the “unsteady” coupled mode to calculate correctly the amplitude and phase of the wing movement. Thus, a fixed support at the wing’s root is assumed while neglecting the elasticity of flange and support. In order to speed up convergence towards steady state, artificial Rayleigh-type structural damping is used. Typical computing time for an inviscid flow simulation using 200 000 grid points on a vector computer with a performance of 1000 MFLOPS is about one hour. An example of results for steady deformations, Fig. 5 shows a comparison of calculated and measured root angles of attack for zero lift. For higher flow speeds, the numerical solution closely approaches the experimental results. The relative differences at lower flow speed are probably due to errors caused by the very low forces to be calculated and measured.

In order to compare numerical and experimental results of dynamic response tests, some examples at higher flow speeds (45 and 65 m/s) were computed at the respective zero lift angles of attack determined previously. In addition to the numerical input data shown in Section 2.3.2, it was essential to determine the aero-structural equilibrium state just before cutting or burning the fiber, particularly the correct value of the fiber force measured. This initial condition for the pluck test had to be determined for the numerical simulation as follows:

Starting with the steady aero-structural solution under the flow conditions specified, the same additional force of $F_f = 50$ N was introduced in both cases by pulling the wing structure with a fiber attached to a pin set close to the leading edge of the wing tip. Under wind-on conditions, this yielded steady deformations (Figs. 7 and 8) for the two different flow speeds. Here, too, artificial damping was used to accelerate convergence towards a new equilibrium.

Making use of the eccentric location of the pin (5% of chord), the fiber was used to create a transverse force and a nose-up torsion moment. The torque acts against the airfoil pitching moment, causing a positive twist of the wing (see

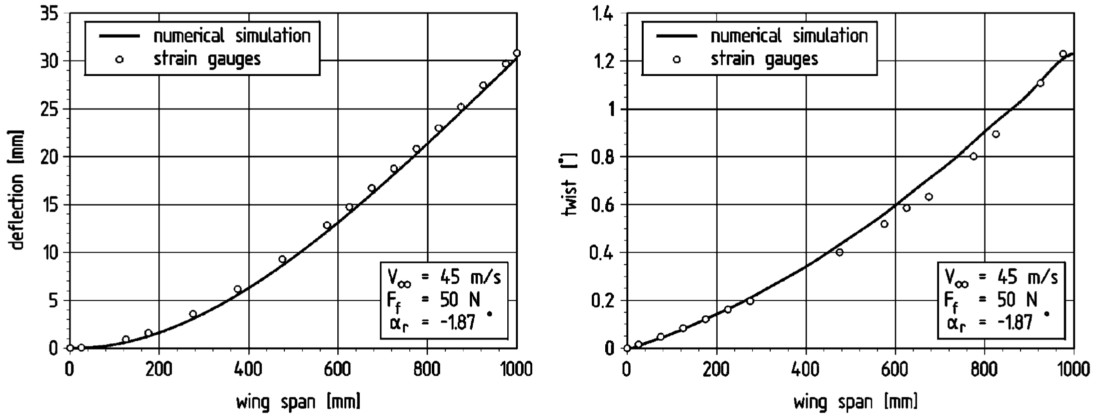

Fig. 7. Initial wing deformation state at $V_\infty = 45$ m/s.

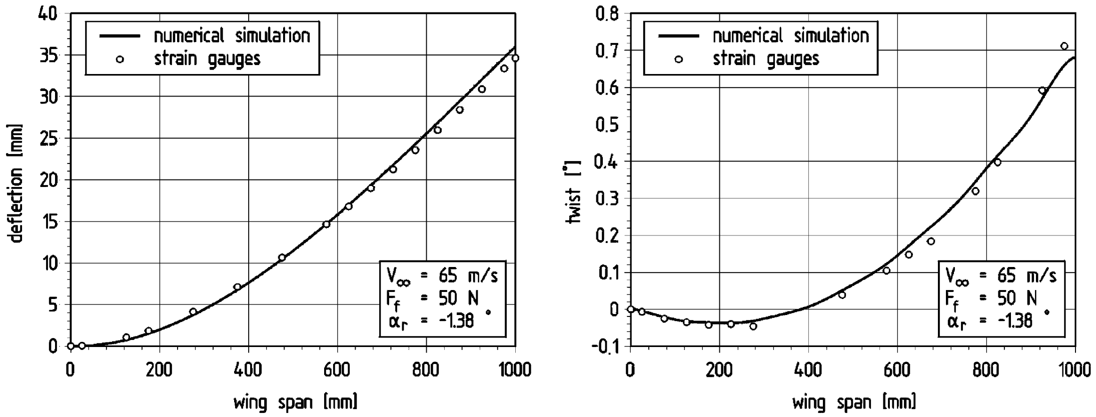

Fig. 8. Initial wing deformation state at $V_\infty = 65$ m/s.

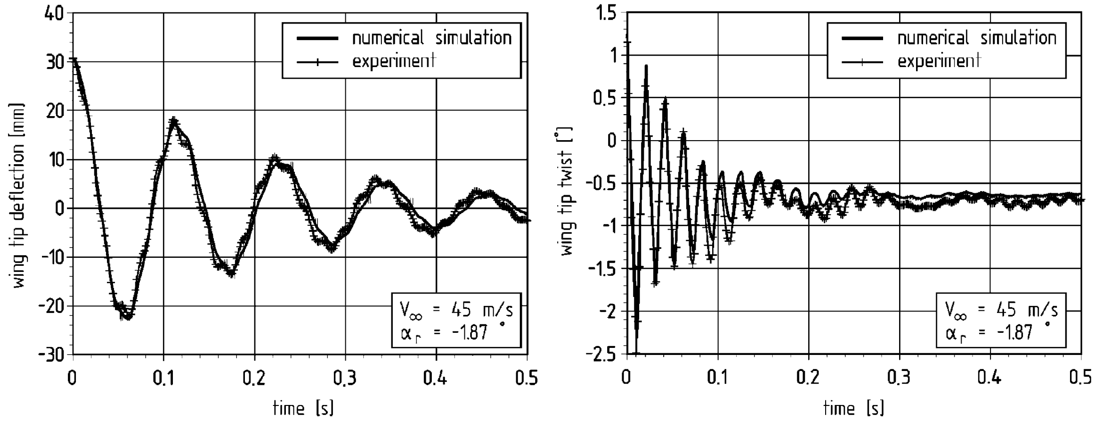

Fig. 9. Wing tip movement at $V_\infty = 45$ m/s.

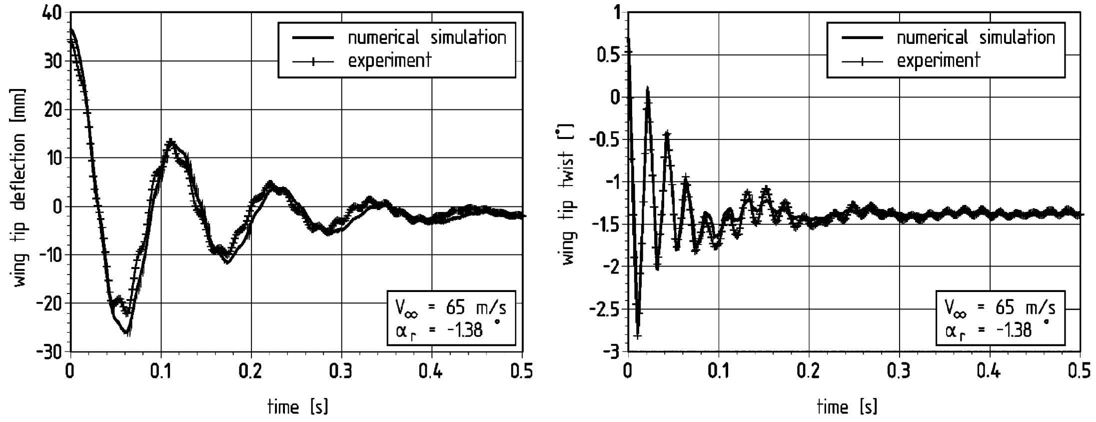

Fig. 10. Wing tip movement at $V_\infty = 65$ m/s.

Figs. 9 and 10, right). Since the profile pitching moment increases with the flow speed, the twist at 65 m/s was lower than at 45 m/s. The wing's deflection was mainly caused by the transverse force of the fiber (Figs. 9 and 10, left). Furthermore, the additional positive twist caused a positive lift, depending on the flow speed. Hence, the deflection at 45 m/s is only slightly smaller than that at 65 m/s.

The simulation data agree well with the experimental data. Several simulations were done with different fiber forces, and hence with different initial deformations, showing low sensitivity of the damping to the amplitude of the initial deformation.

Finally, at time zero, the additional force is removed (i.e., the fiber is burned) and the wing motion is determined in the "unsteady" fluid–structure coupled mode. It was essential that during the test run, the fiber would not become reattached to the wing surface, or the run would have to be repeated.

For comparing the direct aeroelastic simulation with the experiments, the following data were chosen as typical for the dynamic behavior of the elastic wing model:

(i) root section moments in bending and torsion;
(ii) root section force in the lift direction (total lift force);
(iii) wing tip movement (deflection and twist);
(iv) local pressure coefficient (sensors 4 and 7).

The root section moments shown in Figs. 11 and 12 are suitable for separately visualizing the coupled aerodynamic, stiffness and mass forces/moments for the plunge and the torsion movement of the elastic wing model. The results are consistent, there is only a small difference in the cycle duration of the 1st plunge mode. The aerodynamic damping of

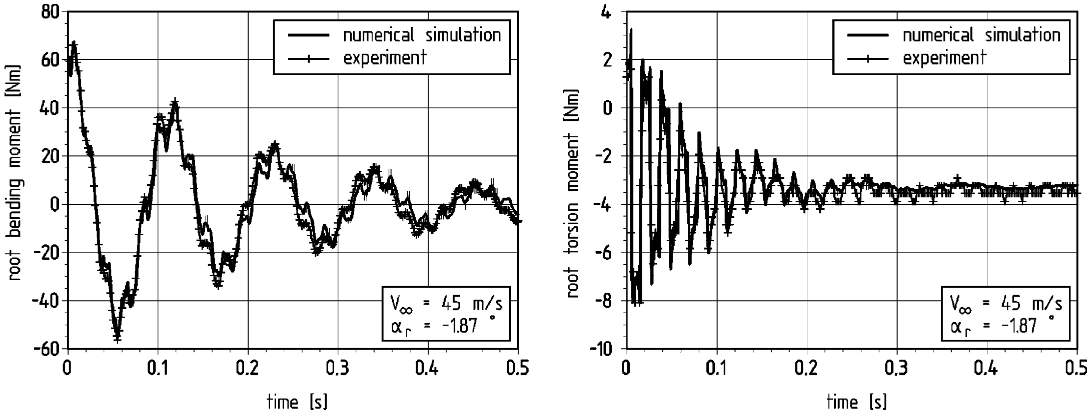

Fig. 11. Root section moments in bending and torsion at $V_\infty = 45$ m/s.

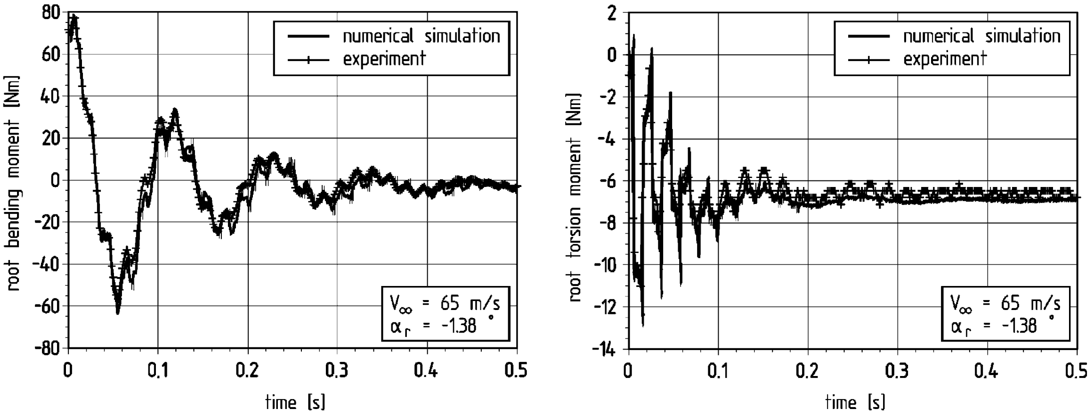

Fig. 12. Root section moments in bending and torsion at $V_\infty = 65$ m/s.

the plunge and the twist motion in particular are reproduced accurately by the numerical simulation for both flow speeds shown here. The assumption that structural damping is negligible compared to the aerodynamic damping, was obviously allowed in the case of this wing model.

Regarding wing tip movement, the results also agree well, except the numerical simulation did not reproduce wing movements precisely due to higher-order vibration modes (Figs. 9 and 10). Discretization of the structure using cubic elements (Friedman and Kosmatka, 1993) or a higher number of beam elements may improve results.

The total lift force shown in the graphs (Figs. 13 and 14, left) again shows the good consistency between experimental and numerical simulation data. The other integral values (above), however, are better for understanding wing motion. The graph represents the superposition of the aerodynamic, elastic and mass forces induced by all the stimulated plunge and torsion modes.

The last values to be compared are the local pressure coefficients at 50% half-span. Figs. 15 and 16 (left) show the pressure distribution calculated for this section and the values measured at discrete points are displayed for a completely decayed oscillation (steady case). A comparison of the graphs (Figs. 13–16, right) with the wing motion (Figs. 9 and 10) clearly shows the influence of the wing's twist and plunge motions. Even though agreement for sensors 4 and 7 at 45 m/s and for sensor 4 at 65 m/s is good, a time-independent difference between simulation and experiment can be seen for the pressure coefficient of sensor 7 at 65 m/s. Because of the specific flow conditions (zero lift) and the sensor position, the constant shift relative to the unsteady amplitudes seems to be large. As for the absolute value, however, the shift turns out to be less than 5% of the dynamic pressure (Fig. 16, left). Nevertheless, the unsteady behavior of the flow during the oscillation at 65 m/s is clearly shown by sensor 7 (Fig. 16, right).

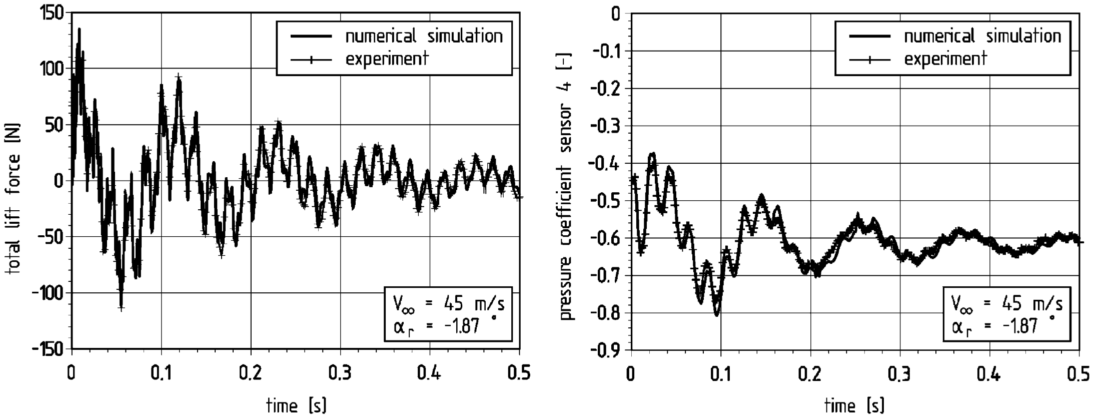

Fig. 13. Total lift force and local pressure (sensor 4) at $V_\infty = 45$ m/s.

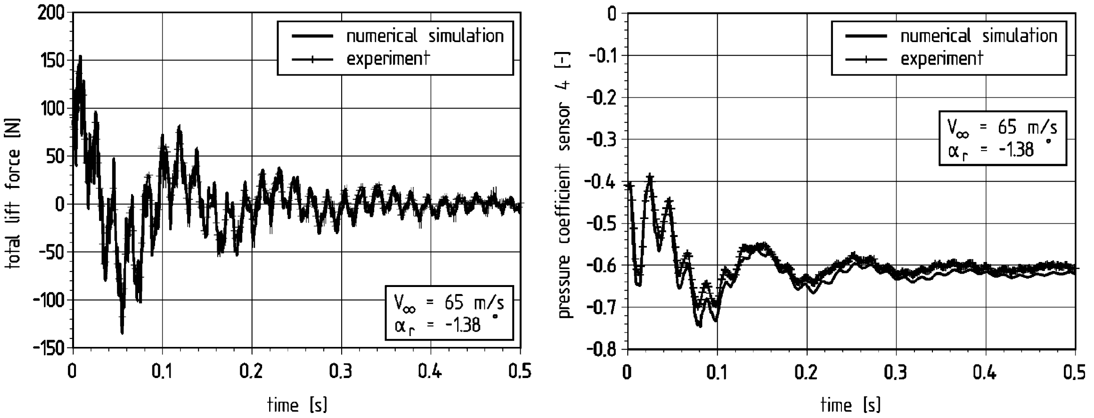

Fig. 14. Total lift force and local pressure (sensor 4) at $V_\infty = 65$ m/s.

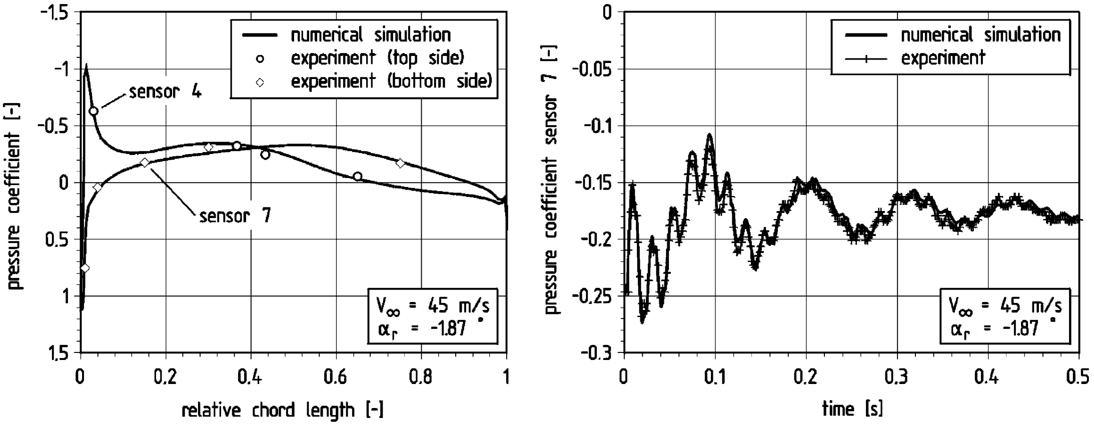

Fig. 15. Pressure distribution (steady case) and local pressure (sensor 7) at $V_\infty = 45$ m/s.

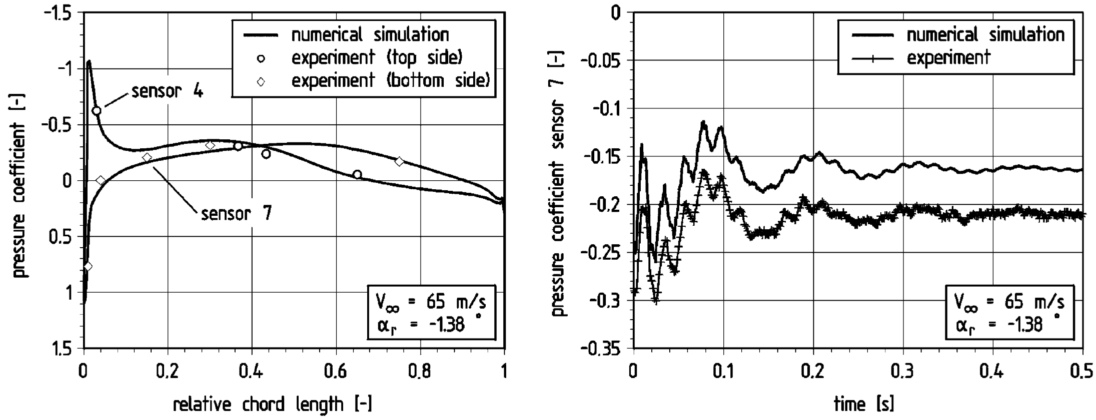

Fig. 16. Pressure distribution (steady case) and local pressure (sensor 7) at $V_\infty = 65$ m/s.

4. Conclusions and outlook

A highly elastic wind tunnel wing model with predefined aerodynamic and structural properties was successfully designed, qualified and tested. It was equipped with several measurement devices and sensors (piezoelectric balance, strain gauges, accelerometers, pressure transducers) to collect data for validation purposes.

Data generated by the direct aeroelastic simulation program SOFIA for the dynamic aero-structural response of a straight-wing model in subsonic flow showed good agreement with experimental data. In order to approximate step-by-step the plan form of a large civil aircraft wing, an elastic back-swept wing model with constant chord was built and qualified under wind-off conditions. First results from numerical simulations and experiments with this swept-wing model are expected soon. Validation will be similar to that for the straight-wing model while stressing the kinematic and structural coupling effects of the back-swept wing model.

Experimental determination of the flutter boundary for different aeroelastic wing models will also be pursued, supplementary to research reported by Eckstrom et al. (1994) and Tang and Dowell (2001). Determination of the behavior of aeroelastic wing models near the flutter boundary will give data for validating the new CFD code for aeroelastic research developed at Aachen University (RWTH) (Fig. 4).

Acknowledgements

This work was supported by the Deutsche Forschungsgemeinschaft (DFG) at the Collaborative Research Center SFB 401 "Flow Modulation and Fluid-Structure Interaction at Airplane Wings" at the Aachen University (RWTH).

References

Amiryants, G.A., Ishmuratov, F.Z., 2001. Multi-purpose modular aerodynamic/aeroelastic model. Proceedings of International Forum on Aeroelasticity and Structural Dynamics, Madrid, pp. 509–518.

Bendiksen, O.O., Hwang, G.-Y., 1997. Nonlinear flutter calculations for transonic wings. Proceedings of CEAS Forum on Aeroelasticity and Structural Dynamics, Rome, pp. 105–114.

Bennett, R.M., Edwards, J.W., 1998. An overview of recent developments in computational aeroelasticity. Proceedings of AIAA Fluid Dynamics Conference, Albuquerque, AIAA 98-2421.

Bennett, R.M., Eckstrom, C.V., Rivera, J.A., Dansberry, B.E., Farmer, M.G., Durham, M.H., 1991. The benchmark models program—description and highlights of initial results. NASA TM-104180.

Brenneis, A., 1989. Berechnung instationärer zwei- und dreidimensionaler Strömungen um Tragflügel mittels eines impliziten Relaxationsverfahrens zur Lösung der Eulergleichungen. Fortschrittberichte VDI Reihe 7: Strömungstechnik 165.

Britten, G., Ballmann, J., 1999. About the uniqueness of aeroelastic solutions of elastic wings in transonic flow. NNFM 72, 77–84.

Britten, G., Ballmann, J., 2000. Navier–Stokes based direct numerical aeroelastic simulation. Proceedings of International Congress of Aeronautical Sciences, Harrogate, Paper No. ICA0483.

Britten, G., Ballmann, J., 2001. Fluid–structure interaction at panels and large span wings with computational aeroelasticity. Proceedings of International Forum on Aeroelasticity and Structural Dynamics, Madrid, pp. 51–62.

Butt, G., Dafnis, A., 1989. The effect of winglets on aircraft wing flutter. Proceedings of European Forum on Aeroelasticity and Structural Dynamics, Aachen, pp. 621–632.

Dafnis, A., Jung, W., Reimerdes, H.-G., 1998. Auslegung elastischer Windkanal-Flügelmodelle zur Validierung aeroelastischer Berechnungen. Proceedings of Aeroelastik-Tagung der DGLR, Göttingen, pp. 261–316.

Eckstrom, C.V., Seidel, D.A., Sandford, M.C., 1994. Measurements of unsteady pressure and structural response for an elastic supercritical wing. NASA Technical Paper 3443.

Farhat, C., Lesoinne, M., 2000. Two efficient staggered algorithms for the serial and parallel solution of three-dimensional nonlinear transient aeroelastic problems. Computer Methods in Applied Mechanics and Engineering 182, 499–515.

Friedman, Z., Kosmatka, J.B., 1993. An improved two-node Timoshenko beam finite element. Computers and Structures 47 (3), 473–481.

Heinrich, R., Pahlke, K., Bleecke, H., 1996. A three-dimensional dual-time stepping method for the solution of the unsteady Navier–Stokes equations. Proceedings of RAS 'Unsteady Aerodynamics' Conference, London, pp. 5.1–5.12.

Kämpchen, M., Jung, W., Dafnis, A., Reimerdes, H.-G., 2000. Design and qualification concepts for flexible wind tunnel wing models. Proceedings of International Congress of Aeronautical Sciences, Harrogate, Paper No. ICA0466.

Kämpchen, M., Dafnis, A., Reimerdes, H.-G., 2001. Aero-structural investigation on highly flexible wind-tunnel wing model. Proceedings of International Forum on Aeroelasticity and Structural Dynamics, Madrid, pp. 519–531.

Kroll, N., Rossow, C.C., Becker, K., Thiele, F., 2000. The MEGAFLOW Project. Aerospace Science Technology, Vol. 4, pp. 223–237.

Lee-Rausch, E.M., Batina, J.T., 1995. Wing flutter boundary prediction using unsteady euler aerodynamic method. Journal of Aircraft 32 (1), 416–422.

Moir, I.R.M., 1994. Measurements on a two-dimensional airfoil with high-lift devices. AGARD-AR-303 2, A1-1-A2-12.

Özger, E., Schell, I., Jacob, D., 2001. On the structure and attenuation of an aircraft wake. Journal of Aircraft 38 (6), 878–887.

Nellessen, D., 1995. Schallnahe Strömungen um elastische Tragflügel. Fortschrittsberichte VDI Reihe 7: Strömungstechnik, Nr. 302.

Tang, D., Dowell, E.H., 2001. Experimental and theoretical study on aeroelastic response of high-aspect-ratio wings. AIAA Journal 39 (8), 1430–1441.

Werle, M., 1997. Gittergenerierung für die Strömungssimulation von elastischen Auftriebskörpern. Diploma Thesis, RWTH Aachen, Germany.

Yates, E.C., 1988. AGARD standard aerolastic configurations for dynamic response-I.-Wing 445.6. AGARD Report No. 765.

Zingel, H., 1991. Measurement of steady and unsteady airloads on a stiffness scaled model of a modern transport aircraft wing. Proceedings of International Forum on Aeroelasticity and Structural Dynamics, Aachen, DGLR Bericht 91-06.